

Molecular simulation of the competitive adsorption of methane and carbon dioxide in the matrix and slit model of shale kerogen and the influence of water

Decheng Zhang^a, Hao Tang^b, Yuqi Song^{c,*}, M.S.A. Perera^d, P.G. Ranjith^c

^a School of Civil and Transportation Engineering, Hebei University of Technology, Tianjin, China

^b China Railway SiYuan Group Engineering Construction Co., LTD, China

^c Deep Earth Energy Research Laboratory, Department of Civil Engineering, Monash University, Victoria, 3800, Australia

^d Department of Infrastructure Engineering, University of Melbourne, Victoria, 3010, Australia

ARTICLE INFO

Keywords:

Competitive adsorption

Kerogen

Water content

Adsorption selectivity

ABSTRACT

Carbon dioxide enhanced shale gas recovery (CO₂-EGR) technology is of great significance for shale gas extraction and carbon dioxide storage in subsurface, which involves the competitive adsorption in shale nanopores. Adsorption comparisons between the kerogen matrix and slit and between the pure gas and gas mixture are conducted in this study. Kerogen matrix and slit models are built with the type II-A kerogen macromolecules and adsorptions of CH₄ and CO₂ are modelled. It is seen: 1) The gas absolute adsorption increases with its molar fraction while decreases with temperature. The Langmuir pressure for CO₂ decreases while that for CH₄ increases with their molar fractions. The adsorption selectivity of CO₂ over CH₄ decreases with the increase in pressure and the CO₂ fraction, while it is higher in the matrix than that in the slit. Water significantly reduces the gas adsorption especially for matrix. 2) CO₂ has high affinity to the Sulfur and Nitrogen functional groups, while CH₄ molecules mainly adsorb on the Sulfur, Nitrogen and Carbon functional groups, While water are strongly bound to the Oxygen functional groups with water cluster formed at high contents. 3) Lower interaction energies are shown in the matrix compared with the slit due to the adsorption superposition, which results in gases preferentially adsorbed in the matrix then on the slit surface in the kerogen slit model. The water interaction energy is lowest due to the hydrogen bond, while the interaction energy of CO₂ is much smaller than that of CH₄ indicating its adsorption advantage.

1. Introduction

Shale gas is a type of clean energy sources compared with coal and oil, and its commercial exploration in North America helps to sustain the increasing energy demand (Singh and Javadpour, 2016). On the other hand, the green-house gas emissions related to the combustion of fossil fuel cause environmental issues. Therefore, the carbon dioxide-enhanced shale gas recovery (CO₂-EGR) technology is proposed to enhance the shale gas production while sequestering the carbon dioxide into tight formations (Neele et al., 2018; Zhang et al., 2020a). The gas pressure decreases during the gas withdraw resulting in the quick production decline, while the injected carbon dioxide maintains the reservoir pressure and displaces the methane through competitive adsorption in shale nanopores as shown in Fig. 1 (Zhang and Cao, 2016;

Kim et al., 2017). However, the nanoscale mechanisms for the competitive adsorptions of fluid mixture in shale nanopores are still unclear.

The shale gas reservoir is buried deep characterized by low porosity and permeability (Zhang et al., 2020a; Zhang et al., 2020b; Zhang et al., 2022a), and most pores are in the nanoscale especially in kerogen. Liu et al. (2016) found the surface areas of pores smaller than 1 nm and between 1 and 4 nm account for 65% and 30% of the total area respectively. The small pore size results in the large specific surface area and strong interactions between gas and the solid surface (Zhang et al., 2022b). The absorbed gas accounts for 20–85% of total gas for five USA shale systems (Curtis, 2002). Carbon dioxide is preferentially adsorbed in shale nanopores compared with methane (Zhou et al., 2019; Carchini et al., 2022; Han et al., 2022; Wu et al., 2022), therefore it is appropriate

* Corresponding author. Deep Earth Energy Laboratory, Department of Civil Engineering, Monash University, Victoria, 3800, Australia.

E-mail address: yuqi.song1@monash.edu (Y. Song).

<https://doi.org/10.1016/j.geoen.2024.213212>

Received 21 February 2024; Received in revised form 19 April 2024; Accepted 4 August 2024

Available online 6 August 2024

2949-8910/© 2024 The Authors. Published by Elsevier B.V. This is an open access article under the CC BY license (<http://creativecommons.org/licenses/by/4.0/>).

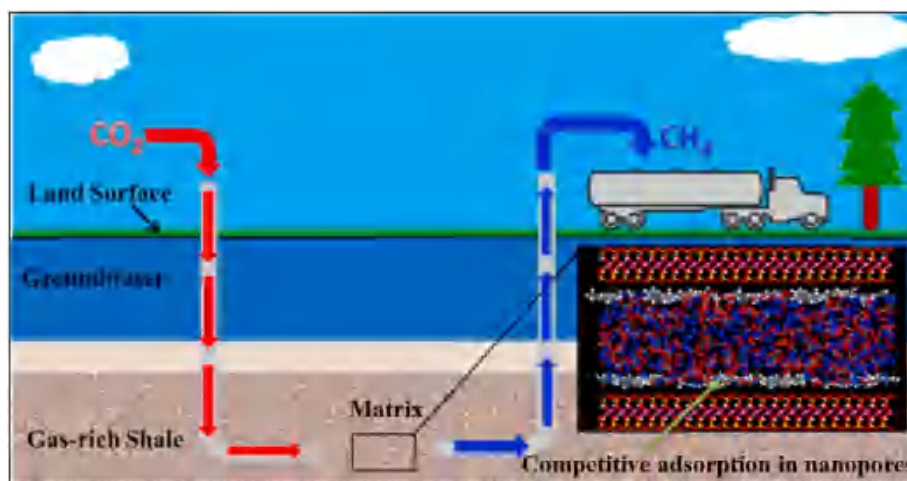


Fig. 1. Schematic of CO₂-EGR (Zhang and Cao, 2016).

for displacing the shale gas. Heller and Zoback (2014) found the adsorption capacity of CO₂ was 2–3 times of that of CH₄ on pure components and real Marcellus and Barnett shale samples. Santos et al. (2018) found the CO₂ molecules had a stronger adsorption affinity for surfaces than hydrocarbon molecules, and the newly formed CO₂ layer appeared to weaken the interaction between the pore surface and shale gas. Xie et al. (2021) quantified the priority adsorption of CO₂ to CH₄ by their absolute adsorption amount ratio, and found the excess adsorption curve of CH₄ was relatively smooth with a maximum of 1.5–2 g/cm³ at 10 MPa for the Longmaxi Shale located in the southern Sichuan Basin. And the temperature had no obvious effect on the shape of CH₄ excess adsorption curve. The excess adsorption curves of CO₂ exhibit sharp peaks at low temperatures (30 and 55 °C), while smooth curves are shown at high temperatures (80 and 100 °C). The adsorption priority coefficient is 2.47–12.16, which increases with pressure but decreases with temperature. It is inferred that the inhibitory effect of temperature on CO₂ priority adsorption is negligible when the temperature is above 80 °C. Qi (2019) found the adsorption amount of CO₂ on shale was about 2.5 times of that of CH₄ with the CO₂ and CH₄ adsorption amounts being 0.339–0.371 mmol/g and 0.134–0.146 mmol/g, respectively. Though the adsorption comparisons between CH₄ and CO₂ are largely investigated, the differences between pure gas and gas mixtures and between matrix and slit need further investigation in terms of gas affinity on the heterogeneous surface, interaction energy, adsorption selectivity and the influence of water.

Zhang and Cao (2016) simulated the displacing process of CH₄ by CO₂ and found the smaller pores have a higher affinity to CO₂ and the replacement efficiency is inversely proportional to pore size. The sequestration of CO₂ increases with the injection pressure, but it decreases with the buried depth under a fixed injection pressure and the displacement efficiency is highest at the depth of 1 km. Sun et al. (2023) built a new molecular dynamics model to simulate the initial displacement stage in the heterogeneous surface pores. Shi et al. (2017) found the CH₄ recovery increased by 12% when the molar volume of CO₂ in the effluent accounted for 10%. Liu et al. (2018) investigated the transport of supercritical CO₂ in silica nano-channels under different pressure gradient by using the non-equilibrium dynamics method, they found the diffusion of supercritical CO₂ increased with the pressure gradient and the channel size. The gas composition and pressure changes during the displacing process, thus it is critical to study the competitive adsorption of fluid mixture in the nanopores under various composition and pressure conditions.

The adsorption experiments conducted on shale core or particles only show the macroscopic behaviors with the nanoscale competitive adsorption mechanism remained unclear. Molecular simulation is an

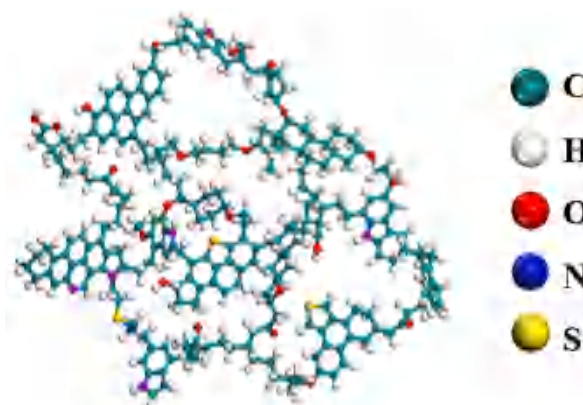


Fig. 2. The structure of II-A Kerogen fragment.

effective method to uncover the nanoscale fluid-rock interactions, which has been used by many researchers (Hu et al., 2022; Sun et al., 2023). However, the adsorption comparisons between kerogen matrix and slit models and between pure gas and gas mixtures need further study. Therefore, real shale kerogen matrix and slit models were constructed in this study, and GCMC and molecular dynamics simulation were conducted to investigate the influences of water and gas compositions on the competitive adsorption in terms of adsorption amount, density distribution, fluid affinity, interaction energy and adsorption selectivity etc.

2. Model and method

2.1. Kerogen model construction

The main component of organic matter in shale is kerogen, which can be divided into three types (Yu et al., 2020): Type I kerogen with the highest hydrogen content (H/C > 1.45) but lowest oxygen content (O/C < 0.04); Type II kerogen is mainly existed in the petroliferous marine shale with more oxygen (O/C > 0.05) but less hydrogen (H/C < 1.05); while Type III kerogen comes from the higher plants in Tertiary and Quaternary shale, which is rich in oxygen (O/C > 0.1) but low in hydrogen (H/C < 1.0). Among them, type II kerogen is considered to be the most common source of unconventional shale gas (Zhao et al., 2017), which is used for the adsorption simulation in this study. Nanoscale kerogen slits were constructed by compressing the kerogen fragments into matrix blocks, which were then separated by a certain slit

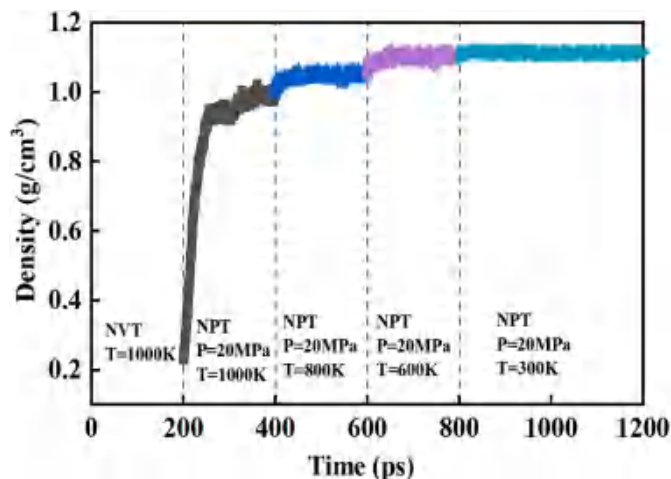


Fig. 3. Density variations during the molecular dynamics simulations.

width. Firstly, the fragment of type II-A kerogen built by Ungerer et al. (2014) with the molecular formula of $C_{252}H_{294}O_{24}N_6S_3$ was constructed as shown in Fig. 2. Geometry optimization and annealing were conducted to minimize the energy of the kerogen fragment and avoid unreasonable atom contacts (Chen et al., 2024). 5 temperature cycles were used for the annealing with the initial and highest temperature being 300 K and 1000 K respectively. Then ten fragments were packed into an amorphous model with a density of 0.1 g/cm³. Five different initial structures were used for modelling to eliminate the uncertainty. Relaxation under 1000 K was first conducted for 200 ps in NVT ensemble, then the molecular dynamics simulation in NPT ensemble were carried out in sequence under temperatures of 1000 K, 800 K, 600 K and 300 K with a pressure of 20 MPa. The simulation runned for 400 ps at 300 K and 200 ps at the other temperatures. The Condensed-phase Optimized Molecular Potentials for Atomistic Simulation Studies (COMPASS) forcefield (Sun, 1998) was used for all the simulations with the pressure and temperature controlled by the Berendsen method and Andersen method respectively. Variations of the kerogen density during the molecular dynamic simulation were shown in Fig. 3. The final kerogen density is 1.126 g/cm³, which is close to the 1.13 g/cm³ measured by Ungerer et al. (2014). The kerogen slit was constructed by separating two parallel matrix blocks by a certain distance. 2 nm slit width was chosen because it is the boundary size between micropore and mesopore and both adsorption phase and free phase gas exist in the 2 nm width slit. Besides, the computation time is also acceptable for this width. The

constructed kerogen matrix model and 2 nm width slit model are shown in Fig. 4.

2.2. Modelling method

The molecular structures of kerogen and adsorbate (CH_4 , CO_2 and H_2O) were first optimized by using the molecular dynamics simulation. The kerogen matrix was fixed with the functional groups nonrotatable during the following adsorption and molecular dynamics simulations. Then the adsorptions of pure gas and gas mixtures with different molar fractions under various temperature (320/360/400K) and pressures (0.1–20 MPa) conditions were modelled by adopting the Grand canonical Monte Carlo (GCMC) method. The first ab initio forcefield COMPASS was used, and the van der Waals and electrostatics interactions were derived by the Atom-based and Ewald summation methods respectively with the cutoff radius being 15.5 Å. Adsorption isotherms were obtained by calculating the adsorption amount under a series of pressures at a constant temperature. Molecular dynamics simulations were conducted on the adsorption configurations in the NVT ensemble with the temperature controlled by the Anderson thermal bath. The total dynamics simulation runned for 1×10^7 steps with a time step of 1 fs, and the first 5×10^6 steps were for equilibration and the other 5×10^6 steps were used for data collection. The water-containing kerogen models were constructed by adding a certain number of water molecules in the kerogen matrix according to the water weight ratio, which is the water mass divided by the total mass of moist kerogen. Then the gas adsorption simulations were conducted.

The potentials of non-bonded interactions for the gas adsorption are mainly composed by the van der Waals (vdW) and electrostatic energies (Coulomb) as shown below.

$$E_{non-bond} = E_{vdW} + E_{coulomb} = \sum_{ij} \epsilon_{ij} \left[2 \left(\frac{r_{ij}^0}{r_{ij}} \right)^9 - 3 \left(\frac{r_{ij}^0}{r_{ij}} \right)^6 \right] + \sum_{ij} C \frac{q_i q_j}{\epsilon_0 r_{ij}} \quad (1)$$

where ϵ_{ij} is the well depth at equilibrium (kcal/mol), r_{ij} is the distance between atom i and j (Å), r_{ij}^0 is the equilibrium distance between atom i and j (Å), $C = 332.0647(kcal/mol)\text{Å}/e^2$ is a unit conversion factor, q_i and q_j are the charges of atom i and j respectively (e), ϵ_0 is the relative dielectric constant. ϵ_{ij} and r_{ij}^0 are calculated by the 6th-power combination rule in COMPASS as shown in Eqs. (2) and (3) respectively.

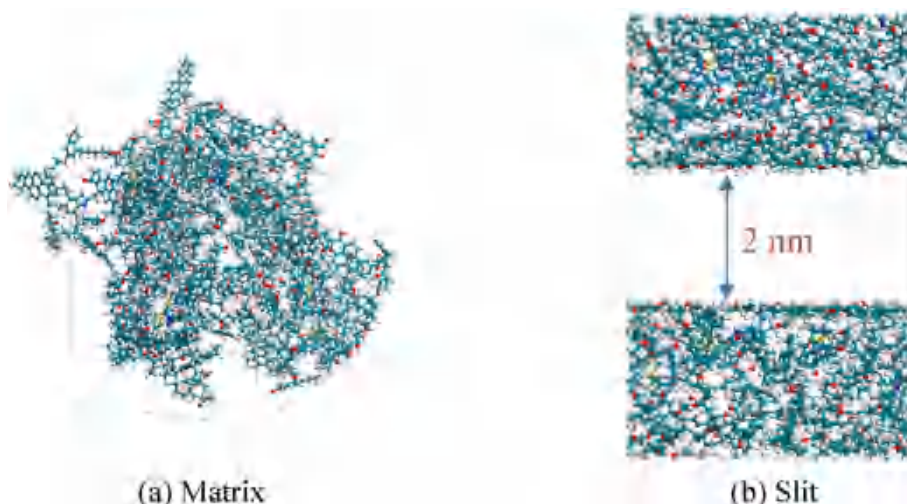


Fig. 4. Kerogen matrix and slit models.

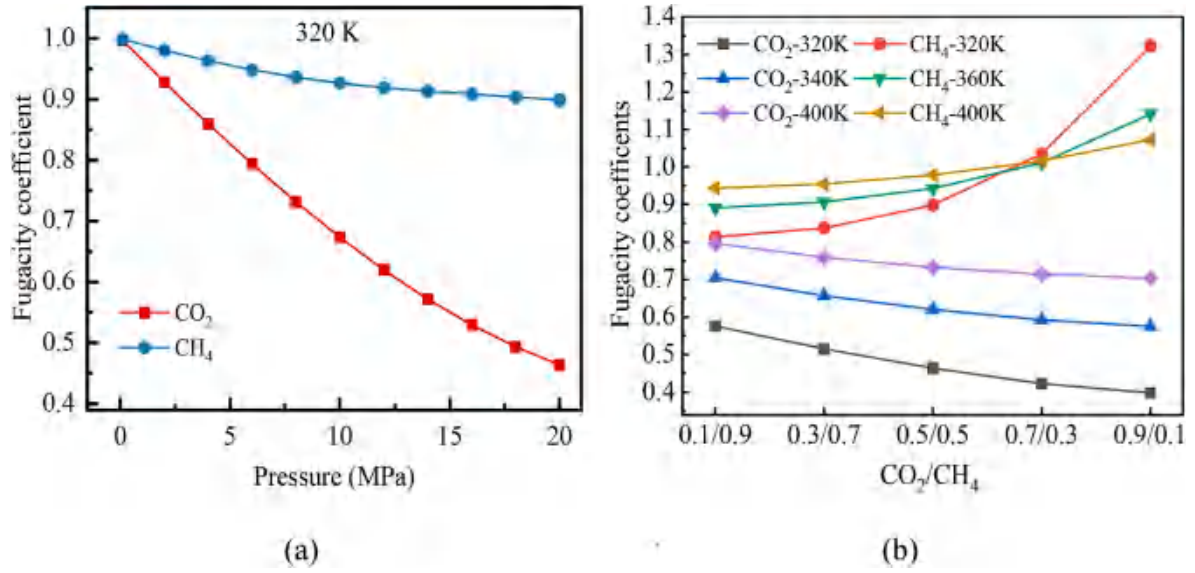


Fig. 5. Fugacity coefficients of each gas component in mixtures (a) Variations with pressure at equimolar ratio at 320 K; (b) Variations with molar fraction under different temperatures at 20 MPa.

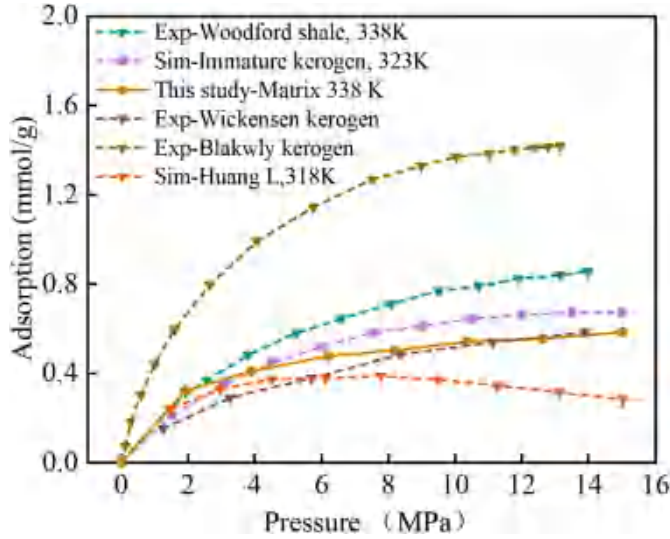


Fig. 6. Adsorption verification with data in literature.

$$\varepsilon_{ij} = \sqrt{\varepsilon_i \varepsilon_j} \frac{2(r_{ii}^0)^3 (r_{jj}^0)^3}{(r_{ii}^0)^6 + (r_{jj}^0)^6} \quad (2)$$

$$r_{ij}^0 = \left[\frac{(r_{ii}^0)^6 + (r_{jj}^0)^6}{2} \right]^{\frac{1}{6}} \quad (3)$$

The gas chemical potential in the GCMC simulations can be derived by the gas fugacity, which is the product of gas pressure and fugacity coefficient.

$$\mu = \mu_0 + RT \ln \frac{f}{p_0} \quad (4)$$

$$f = p\varphi \quad (5)$$

Where μ_0 and p_0 are the gas reference chemical potential (kJ/mol) and pressure (MPa) respectively, f is fugacity (MPa), T is the temperature (K)

and φ is the fugacity coefficient.

The fugacity coefficient (φ) is unity for ideal gas but it is usually lower for real CH₄ and CO₂ gases under high pressures, which is calculated by the GERG-2008 equation of state embedded in the REFPROP software. The GERG-2008 EOS is suitable for natural gases and other mixtures, which is based on the multi-fluid approximation explicit in the reduced Helmholtz free energy (Kunz and Wagner, 2012). The calculated fugacity coefficient for each component in the gas mixtures under different pressure, temperature and molar fractions are shown in Fig. 5. The fugacity coefficient of either CH₄ or CO₂ decreases with increases in pressure at equimolar compositions as shown in Fig. 5 (a), and much larger reductions are observed for CO₂. While the fugacity coefficient of each gas component also decreases with the increase in its molar fraction as indicated in Fig. 5 (b). The fugacity coefficient of CO₂ increases with temperature, while that of CH₄ decreases with temperature at small molar fractions and increases with temperature at molar fractions above 0.5. It should be notified that the fugacity coefficients of CH₄ are always higher than those of CO₂ in this study.

CH₄ adsorption simulation on the kerogen model was conducted and compared with data in literature (Rexer et al., 2014) to verify the accuracy of the built matrix model as shown in Fig. 6. It is seen that the adsorption amount of our kerogen model matches the data measured by other researchers.

3. Results and analysis

3.1. Competitive adsorption in kerogen matrix

3.1.1. Adsorption isotherms

The GCMC method was used to simulate the adsorption of the mixtures of CO₂ and CH₄ with different molar ratios in the kerogen matrix at 320/360/400 K with the pressure ranging from 0.1 to 20 MPa. The adsorption amount on the amorphous kerogen structure is expressed as the adsorbate amount per unit mass of adsorbent (mmol/g). Adsorption isotherms of each gas component are plotted in Fig. 7 and fitted by using the Langmuir equation, which has been commonly used in literature (Tang et al., 2024).

$$n = \frac{n_L p}{p + P_L} \quad (6)$$

Where n is the adsorption amount, n_L is the Langmuir amount repre-

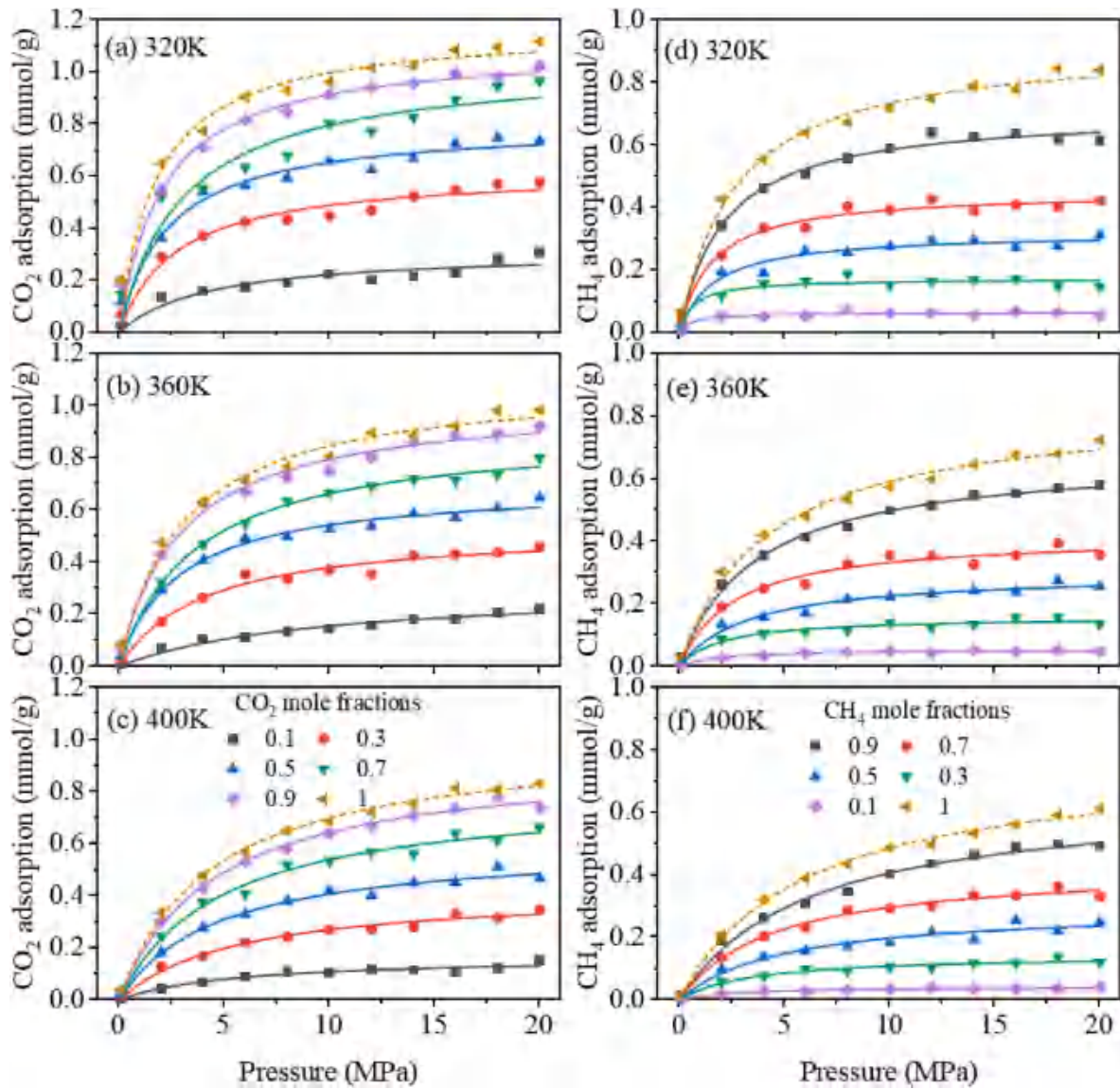


Fig. 7. Adsorption isotherms of gas mixture on the kerogen matrix.

sending the maximum adsorption amount, P_L is the Langmuir pressure which corresponds to the pressure at half of the maximum adsorption amount.

Both the adsorptions of CO_2 and CH_4 belong to the type I isotherm with the adsorption amount increasing significantly initially followed by a gentle increase at high pressures. The absolute adsorption of each gas

component increases with its molar fraction, while it decreases with the increase of temperature. The gas adsorption is positively related to the fugacity, which increases with the molar fraction under a certain pressure. While adsorptions of CH_4 and CO_2 on kerogen are physical adsorption, and the intense thermal motions of gas molecules at higher temperatures make gas molecules escape from the kerogen surface and

Table 1

Fitting parameters of Langmuir equation for adsorptions in kerogen matrix.

T		CO ₂ molar fraction						CH ₄ molar fraction					
		0.1	0.3	0.5	0.7	0.9	1	0.1	0.3	0.5	0.7	0.9	1
320K	P_L	4.20	2.72	2.30	3.05	2.04	1.75	0.62	0.66	1.64	1.54	2.12	2.63
	n_L	0.31	0.62	0.80	1.04	1.10	1.17	0.06	0.17	0.32	0.45	0.71	0.93
	R^2	0.95	0.96	0.96	0.91	0.97	0.96	0.85	0.89	0.95	0.98	0.99	0.99
360K	P_L	6.42	4.08	2.84	3.71	2.92	3.02	1.84	2.01	3.29	2.62	3.63	4.14
	n_L	0.30	0.53	0.67	0.91	1.03	1.10	0.05	0.16	0.30	0.42	0.68	0.84
	R^2	0.97	0.97	0.99	0.99	0.99	0.99	0.97	0.94	0.97	0.97	0.99	0.99
400K	P_L	7.49	5.70	4.67	4.79	4.53	4.33	2.73	3.41	4.89	4.44	6.14	5.82
	n_L	0.17	0.42	0.60	0.80	0.93	1.00	0.05	0.15	0.30	0.43	0.66	0.77
	R^2	0.95	0.98	0.98	0.99	0.99	0.99	0.94	0.96	0.95	0.99	0.99	0.99

Note: Units of P_L and n_L are MPa and mmol/g respectively.

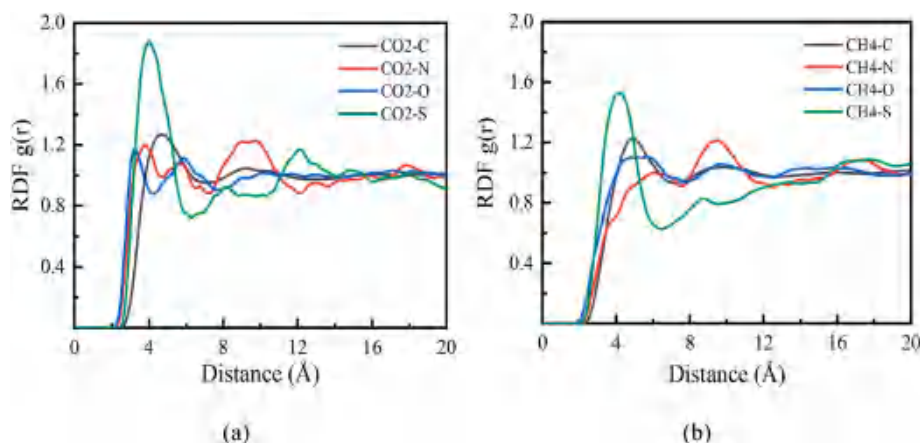


Fig. 8. RDF of pure gas in kerogen matrix at 320 K and 10 MPa.

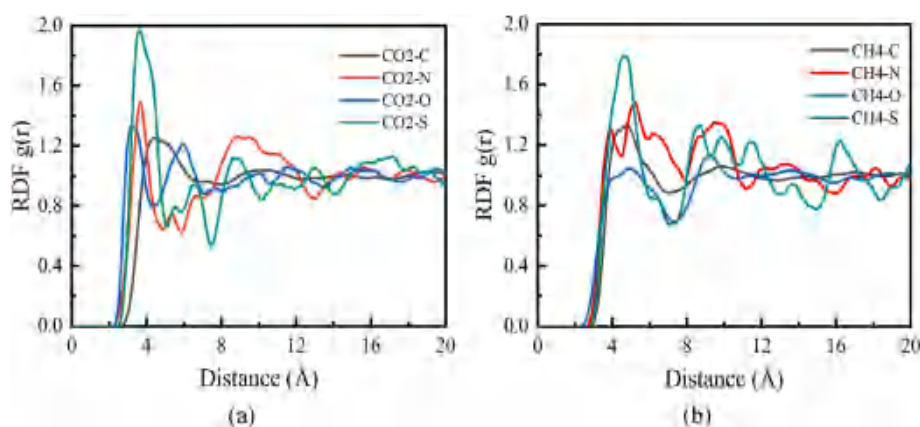


Fig. 9. RDF of gas mixture with equimolar ratio in kerogen matrix at 320 K and 10 MPa.

remain at the free state, which reduces the adsorption capacity. Besides, the gas density also reduces with the increase of temperature according to the ideal gas law. It should be noted that the adsorption capacity of CO₂ on kerogen matrix is much larger than that of CH₄, which is caused by the smaller CO₂ molecular size and stronger interactions with shale (Zhou et al., 2019). The adsorption amounts of CO₂ and CH₄ are 0.719 mmol/g and 0.294 mmol/g respectively under 20 MPa at 320 K at equal molar ratios. The adsorption amount of CH₄ decreases by 31.4% when

the molar fraction of CO₂ increases from 0.1 to 0.3 at 320 K, while a further 17.7% reduction occurs with the CO₂ molar fraction increasing from 0.3 to 0.5, which shows that the CO₂ displacing efficiency decreases with the increase in its molar fraction.

The Langmuir adsorption amounts (n_L) for both CH₄ and CO₂ increase with the molar fraction, while they decrease with temperature (Table 1). And the n_L for CO₂ is more sensitive to the temperature with the n_L decreasing by 25.9% and 10.5% for CO₂ and CH₄ respectively with the temperature increasing from 320 K to 400 K. The Langmuir pressure (P_L) for CO₂ generally decreases with the increase of molar fraction, while the P_L for CH₄ increases with its molar fraction. Adsorption of CO₂ becomes equilibrated at lower pressures when its molar fraction is high as it is preferentially adsorbed compared with CH₄, while the weak adsorption affinity of CH₄ results in the larger P_L at higher molar fractions. P_L for both CH₄ and CO₂ increases with the temperature indicating the inhibiting effects of high temperature on the gas adsorption.

3.1.2. Radial distribution function

In order to find out the adsorption affinity of different gases to the functional groups of kerogen, the radial distribution function (RDF) of gases to the chemically heterogeneous surface are plotted as shown in Figs. 8 and 9 respectively. Pure CH₄ or CO₂ is preferentially adsorbed on the Sulfur-containing functional group at 320 K and 10 MPa as shown in Fig. 8, and the amplitude of CO₂ is higher than that of CH₄ demonstrating the larger adsorption capacity of CO₂. The adsorption peaks for the Carbon-containing functional group are second highest for both pure CO₂ and CH₄, while the second adsorption layers are observed around

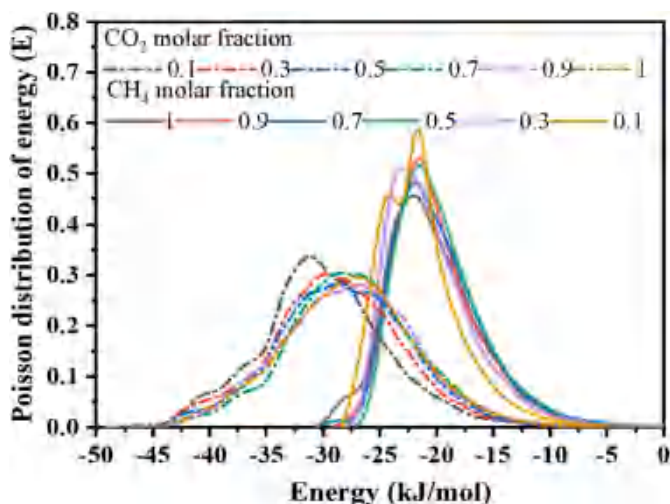


Fig. 10. Gas energy distribution with different molar fractions.

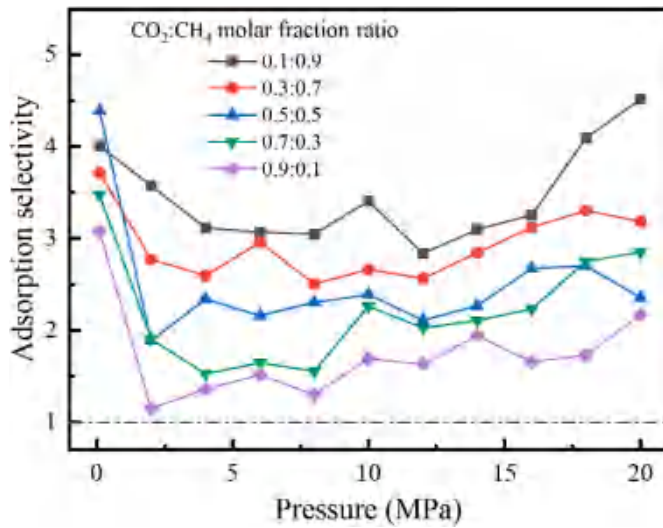


Fig. 11. Adsorption selectivity coefficient of CO₂ over CH₄ in kerogen matrix.

the Nitrogen- and Oxygen-containing functional groups for CO₂. It is also noticed that the first adsorption layer is not obvious for CH₄ on the Nitrogen-containing functional groups.

Compared with the adsorption of single gas component, the amplitude of the first CO₂ adsorption layer increases near the Sulfur-, Nitrogen- and Oxygen-containing functional groups, while the adsorption peaks of CH₄ also increase at the Sulfur- and Nitrogen-containing functional groups but decrease around the Oxygen-containing functional group. This indicates that the CH₄ at the Oxygen-containing functional group is replaced by CO₂. The higher adsorption peaks around the Sulfur- and Nitrogen-containing functional groups for both CO₂ and CH₄ in the mixture compared with the pure gas conditions are due to the higher $g(r)$ values at smaller composition ratios, which have been reported by many researchers (Di Biase and Sarkisov, 2015; Yang et al., 2015).

The energy distributions of CH₄ and CO₂ in the mixture with different molar fractions are shown in Fig. 10. Single peaks are displayed for the energy distributions of both CH₄ and CO₂ indicating that there is only one main interaction type for gas molecules with the kerogen matrix. The interaction energies for CH₄ and CO₂ with the kerogen matrix are around -22 kJ/mol and -28 kJ/mol respectively, which shows the adsorption affinity of CO₂ to kerogen is larger than that of CH₄. The larger binding energy between CO₂ and kerogen is also

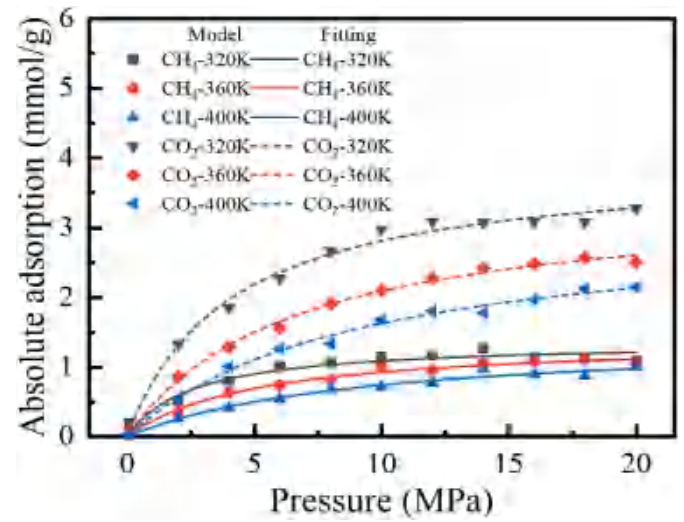


Fig. 13. Absolute adsorptions of CH₄ and CO₂ mixture at equimolar ratios in the 2 nm kerogen slits under different temperatures.

reported by other researchers (Wang et al., 2018; Shi, 2019; Ansari et al., 2022), which is consistent with the larger adsorption capacity of CO₂ in section 3.1.3. The energy distribution curves for CH₄ and CO₂ shift slightly to the right with the increase of their molar fractions, which indicates that gas molecules occupying the adsorption sites in the order of interaction energy.

3.1.3. Adsorption selectivity

The difference in the gas adsorption ability can be quantified by the adsorption selectivity coefficient, which is defined as the quotient of molar fraction ratio of the adsorbed phase to that of bulk phase as shown in Eq. (2) (Zeng et al., 2018).

$$S_{CO_2/CH_4} = \frac{(y_{CO_2}/y_{CH_4})_{adsorbed}}{(x_{CO_2}/x_{CH_4})_{bulk}} \quad (7)$$

Where y_i and x_i are the gas molar fractions in the adsorbed phase and bulk phase respectively.

Fig. 11 shows the changes of the adsorption selectivity coefficient of CO₂ to CH₄ (S_{CO_2/CH_4}) with pressure and the molar fraction ratio. The selectivity coefficient is always larger than unity indicating the higher adsorption capacity of CO₂, which is consistent with the adsorption amount and adsorption energy described above. The adsorption

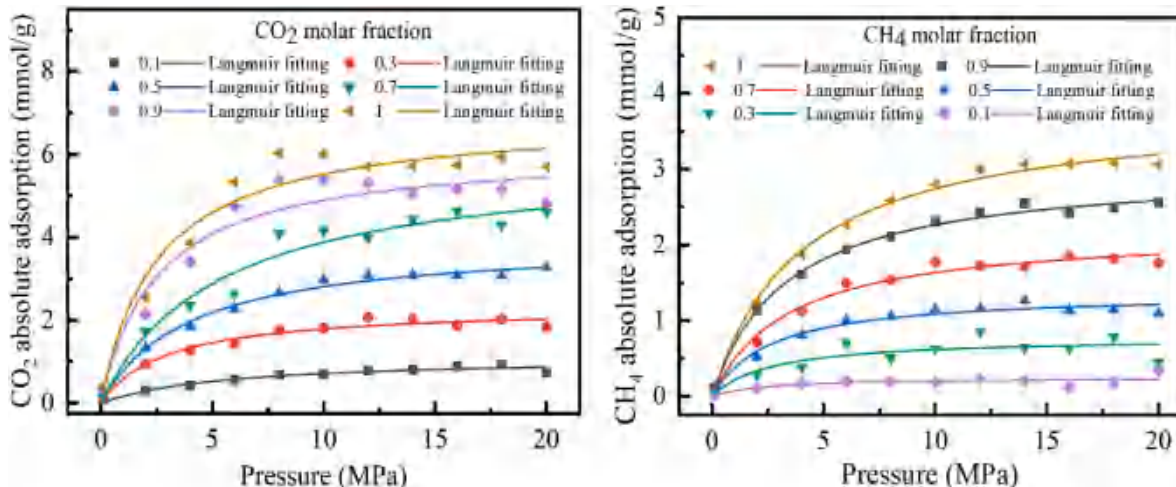


Fig. 12. Absolute adsorption isotherms of pure gas and gas mixture in the 2 nm kerogen slits at 320K.

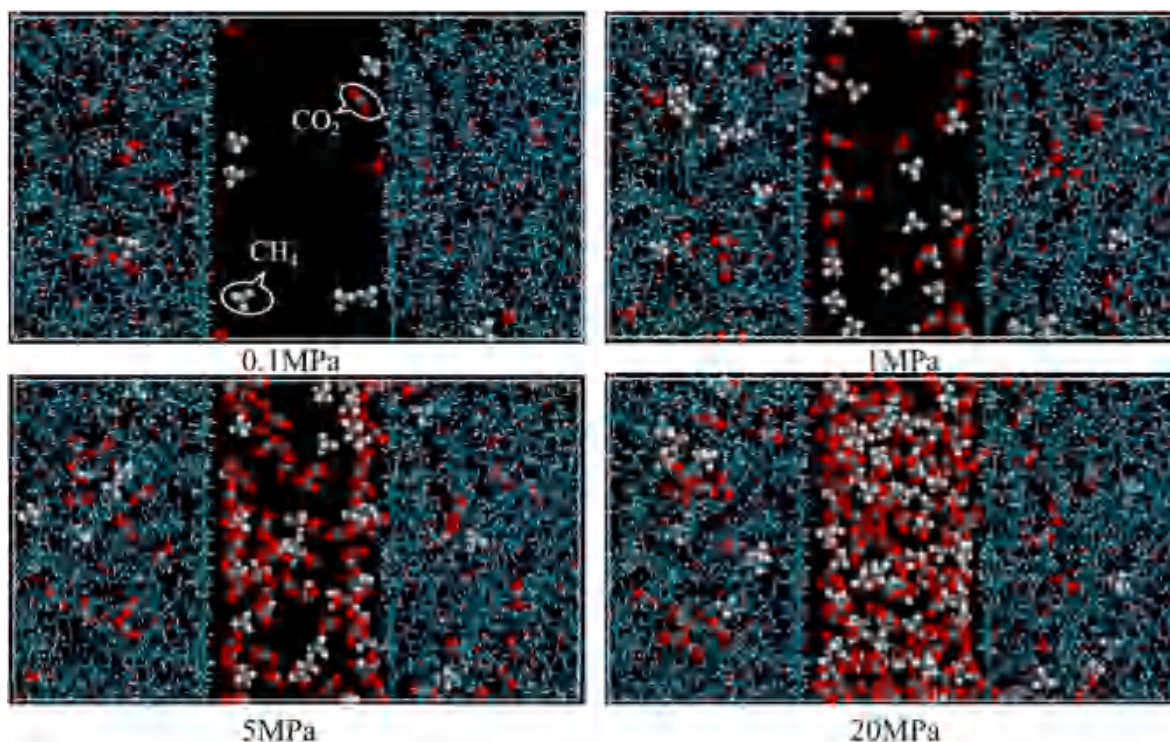


Fig. 14. Adsorption configurations of CH_4 and CO_2 mixture with equimolar fractions in kerogen slit.

selectivity coefficient decreases with the increase in CO_2 molar fraction. This is because CO_2 is first adsorbed onto the Sulfur- and Nitrogen-containing functional groups accompanied by large adsorption heat, and then they are adsorbed on the weak adsorption sites with the increase of its molar fraction resulting in the smaller selectivity coefficients. While the selectivity coefficient first decreases then increases with pressure for all molar fraction compositions. The high adsorption selectivity coefficients at low pressures are because CO_2 is preferentially adsorbed to the limited sites with large interaction energies like the Sulfur-containing functional group, while CH_4 molecules are displaced by CO_2 from the preferred adsorption sites under high pressures resulting in the large adsorption selectivity coefficients.

3.2. Competitive adsorption in kerogen slits

3.2.1. Adsorption isotherms

The absolute adsorptions of pure gas and gas mixtures in the 2 nm width kerogen slit at 320 K are shown in Fig. 12. Type I isotherms are shown for CH_4 and CO_2 with the absolute adsorption amount increasing with the molar fraction. The CO_2 adsorption capacity is higher than that of CH_4 with the absolute adsorption of CO_2 being 1–2 times of that of CH_4 at equal molar ratio as shown in Fig. 13. The adsorption capacity in slit is higher than that in matrix as the large slit surface providing abundant adsorption sites. The absolute adsorption decreases with the increase in temperature, especially for CO_2 . The adsorption amounts reduce by 34.5% and 9% for CO_2 and CH_4 respectively at equimolar ratios under 20 MPa when the temperature increases from 320 K to 400 K.

3.2.2. Density distributions

The adsorption configurations of CH_4 and CO_2 equimolar gas mixtures under different pressures in the 2 nm kerogen slit are shown in Fig. 14. Gas mixtures are adsorbed in the kerogen matrix and on the slit surface at 0.1 MPa with CO_2 and CH_4 mainly distributed in the matrix pores and on the slit surface respectively. Free phase gas starts to form in the slit center at 1 MPa with competitive adsorption of CH_4 and CO_2

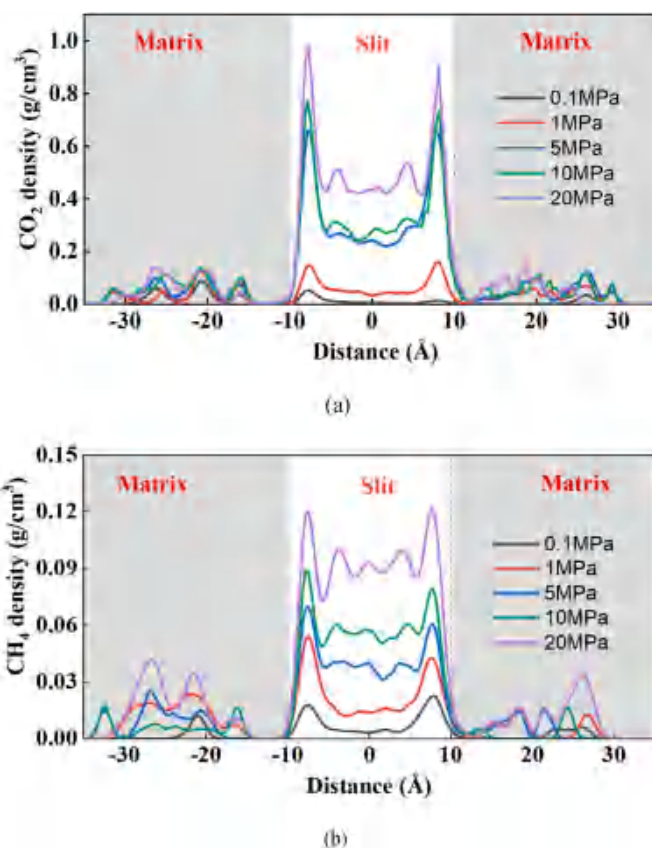


Fig. 15. Density distribution of CH_4 and CO_2 equimolar gas mixture in kerogen slit.

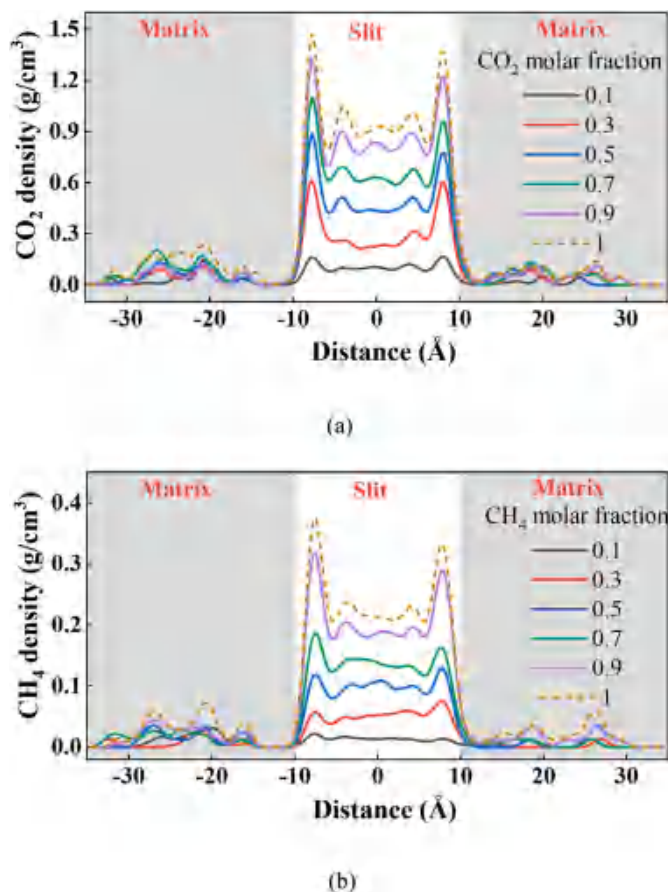


Fig. 16. Density distribution curves of CH₄ and CO₂ with different molar fractions at 20 MPa.

occurring in matrix pores and on the slit surfaces. The adsorption in the matrix becomes almost saturated at 5 MPa while obvious adsorption layers form in the slit which is mainly composed by CO₂ and the amount of free gas also increases in the slit center. The free gas density increases significantly and the slit surfaces are fully covered by the adsorbed gas with the pressure increasing from 5 MPa to 20 MPa, and the density differences between the free gas and the adsorbed phase become smaller. While little increases are observed for gases in the matrix as adsorption in matrix is easier and lower saturation pressures are shown compared with the slit. Density distributions are obtained from the adsorption configurations under different pressures as shown in Fig. 15. In general, gases preferentially fill the matrix pores followed by being adsorbed on the slit surface and finally stored as free phase in the slit center at high pressures. Densities for both CO₂ and CH₄ increase with pressure. It is seen that CO₂ is mainly distributed in the matrix pores while CH₄ is mostly adsorbed on the slit surface at 0.1 MPa. Significant increase in the adsorbed phase density of CO₂ occurs at 5 MPa corresponding to its saturation pressure in the kerogen matrix, which is followed by gentle increases with further pressure increases. While the adsorbed phase density of CH₄ increases steadily as the pressure increases. This certifies that the adsorption of gases with stronger interactions are saturated under lower pressures. Densities in the kerogen slits surpass those in the matrix at 1 MPa and their differences enlarge with the further pressure increases. Large density gaps between the free phase and the adsorbed phase of CO₂ always exist in the slit even at high pressures (Zhou et al., 2019; Lyu et al., 2022), while the density difference becomes small for CH₄ at 20 MPa. This indicates that CO₂ has higher adsorption affinity to kerogen compared with CH₄ resulting in weak CH₄ adsorption layers formed near the slit surface. It is also notified that CO₂ density is much higher than that of CH₄ with the

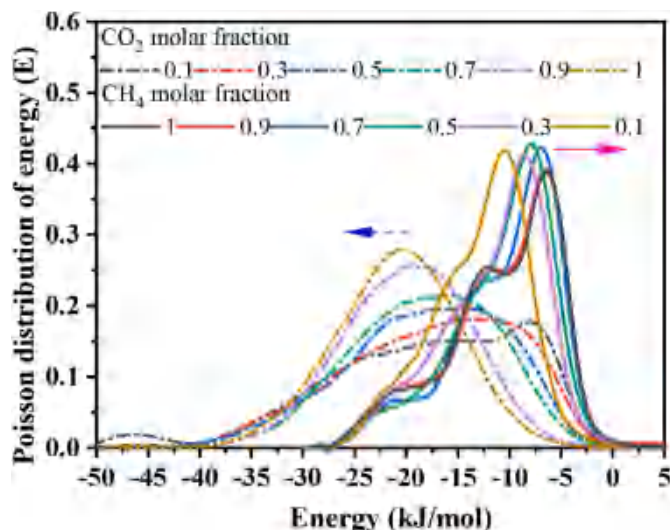


Fig. 17. Energy distribution curves of each gas component in kerogen slit.

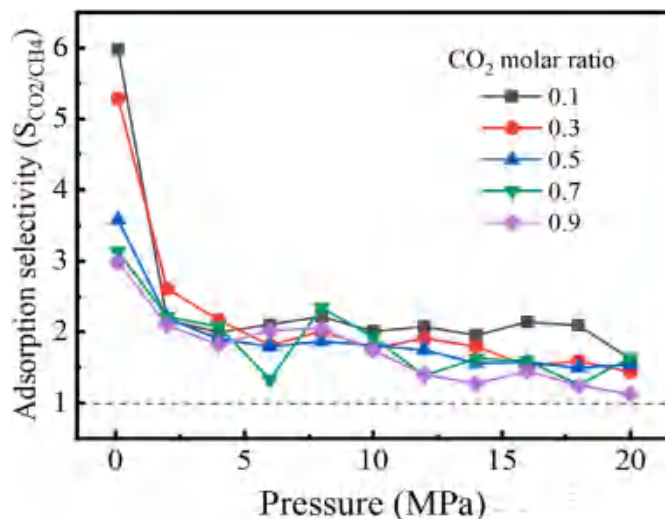


Fig. 18. Adsorption selectivity coefficient of CO₂ to CH₄ in kerogen slit.

adsorbed phase density near the slit surface being 0.93 g/cm³ and 0.12 g/cm³ respectively for CO₂ and CH₄ at 20 MPa. Though the molar mass of CO₂ is 2.75 times of CH₄, the number density of adsorbed CO₂ phase at 20 MPa is still 2.82 times of that of CH₄.

Density distribution curves at 20 MPa are plotted in Fig. 16 to reveal the existence of gas mixtures in kerogen slits. Gas densities in the slits are much higher than those in the matrix for both gases except at 0.1 M fractions, and the gas density increases significantly with its molar fraction especially in the slits. The CO₂ density is lower than that of CH₄ at the CO₂ molar fraction of 0.1, while it becomes higher at the CO₂ molar fraction of 0.3 with the peak density being 0.6 g/cm³ and 0.19 g/cm³ respectively for CO₂ and CH₄, and their density gap enlarges with the further increase of CO₂ molar fraction. Second adsorption layers start to form at the molar fractions of 0.5 and 0.9 respectively for CO₂ and CH₄, and large density gaps between the adsorbed phase and free phase occur at 0.3 and 0.9 respectively for CO₂ and CH₄. Both the early formation of second CO₂ adsorption layer and the large density gap indicate the stronger adsorption affinity of CO₂ to kerogen.

The interaction energy distributions of CH₄ and CO₂ in kerogen slits are shown in Fig. 17. Single-peak curves are shown with the interaction energies for CO₂ being smaller than those of CH₄. The corresponding interaction energies for curve peaks of CO₂ decrease from -8 kJ/mol to

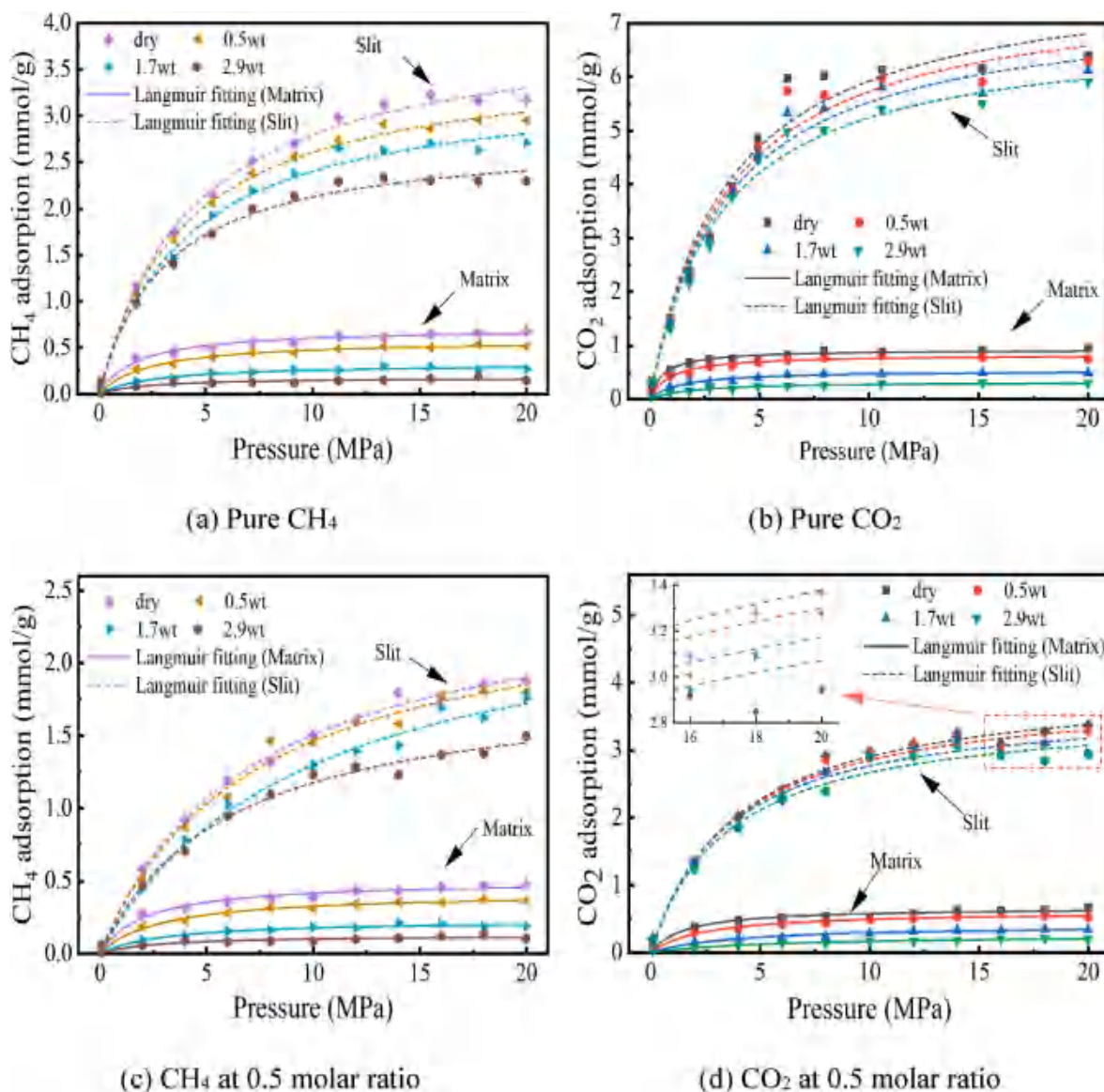


Fig. 19. Effects of water on the adsorptions of pure gas and gas mixture in the kerogen matrix and slit.

−21 kJ/mol with the CO_2 molar fraction increasing from 0.1 to 1.0, while energy of CH_4 molecules increases from −11 kJ/mol to −6 kJ/mol with the increase of CH_4 molar fraction. The competitive adsorption becomes intense with the increase of CO_2 molar fraction resulting in its lower interaction energies, while the increase of the CH_4 fraction induces the gentle increase in the adsorbed gas energy due to its lower adsorption affinity.

3.2.3. Adsorption selectivity

The adsorption selectivity coefficient in the slit is more sensitive to the pressure compared with that in the matrix. Significant reductions occur at low pressures followed by gentle decreases with further pressure increase, however they are always larger than unity indicating the higher adsorption affinity of CO_2 compared with CH_4 (see Fig. 18). High adsorption selectivity coefficients at low pressures indicate the large displacing efficiency at shallow reservoirs. While the adsorption selectivity coefficient also reduces with the increase of CO_2 molar fraction. CO_2 molecules are preferentially adsorbed on sites with lower interaction energies like the Sulfur-containing functional group resulting in the high adsorption selectivity coefficients at low pressures or small CO_2 molar fractions.

3.3. Influence of water on the gas adsorption

3.3.1. Adsorption isotherms

The absolute adsorptions of CH_4 and CO_2 in the kerogen matrix and slit with different water contents are shown in Fig. 19. Both the adsorption amounts of CH_4 and CO_2 decrease with the increase in water content, and the water influence is larger in the matrix than that in the slit. For example, the adsorption of pure CH_4 reduces by 6.9%, 14.5% and 27.5% at the water contents of 0.5 %, 1.7% and 2.9% respectively under 20 MPa in the slit compared with the dry condition, while the decreases are 24.3%, 59.9% and 78% respectively in the matrix. This is because water is preferentially adsorbed in matrix pores reducing the space for gas adsorption. And the CH_4 adsorption is more sensitive to the water content with its adsorption under 20 MPa reducing by 20.3% and 78% in the slit and matrix respectively at the water content of 2.9% compared with 12.7% and 64% for CO_2 . The large decrease of CH_4 adsorption in the water-containing kerogen is that water mainly occupies the sites for CH_4 adsorption and CO_2 molecules can be adsorbed onto the water surface due to the quadrupole moment effect. Besides, the linear structure and smaller size of CO_2 molecule also contribute to the smaller reduction of CO_2 adsorption in the water-containing

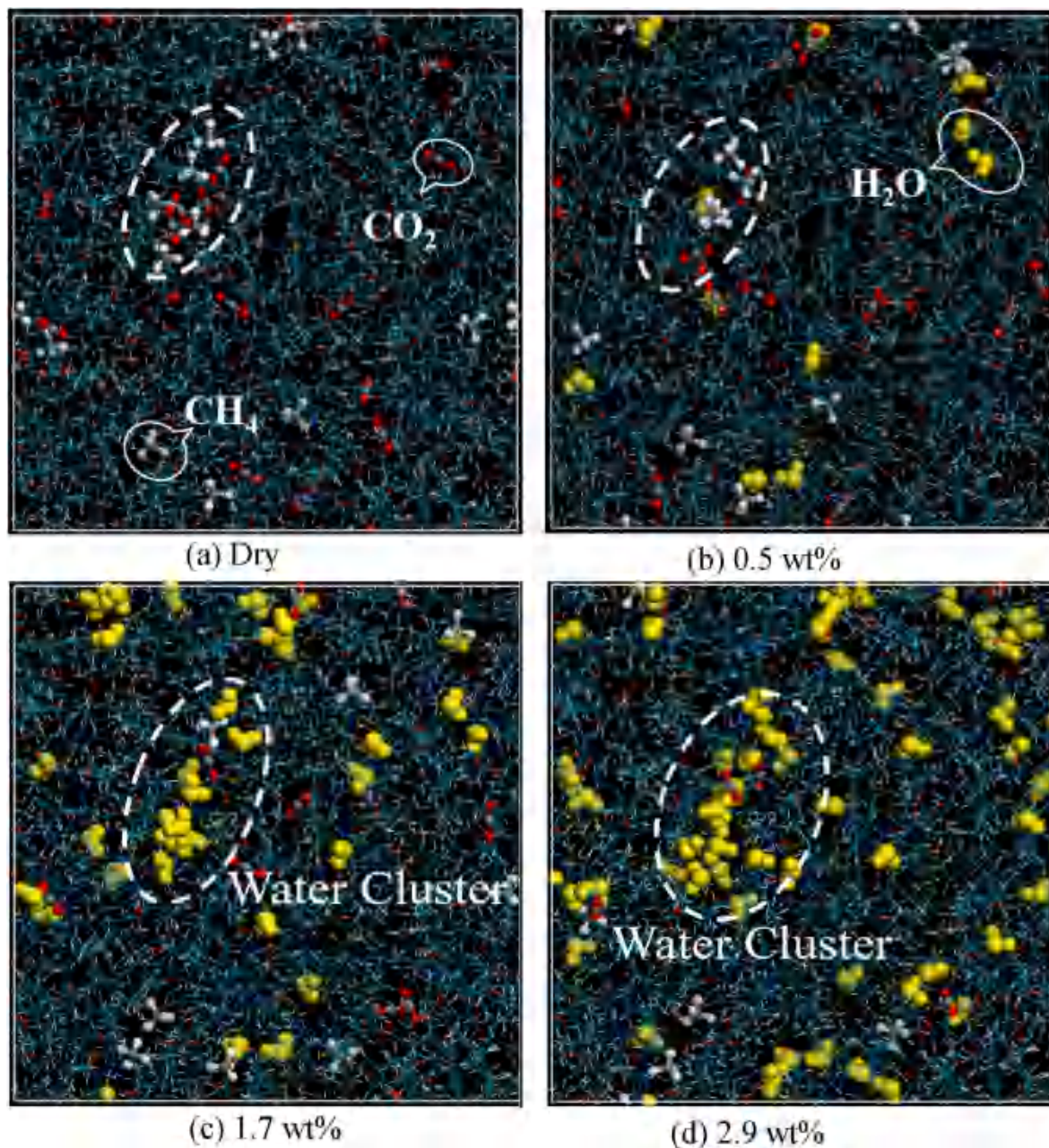


Fig. 20. Distribution of fluid molecules in the kerogen matrix at 20 MPa.

nanopores.

3.3.2. Fluid molecule distributions

Gas mixture and water distributions in the kerogen matrix and slit at 20 MPa are shown in Figs. 20 and 21 respectively. CO_2 and CH_4 are adsorbed in the nanopores of kerogen matrix, and the gas molecules are gradually displaced by water molecules with the increase of water content. Most water molecules are adsorbed in the matrix pores at the water content of 0.5% due to the large adsorption potentials in nanopores, and water clusters are formed at the water contents of 1.7% and 2.9% in the matrix. Majority of the adsorbed CH_4 and CO_2 molecules are displaced by water molecules, which is consistent with the large gas adsorption reductions in the matrix in section 3.3.1. Though most water molecules are adsorbed in the matrix for the slit model at the 0.5% water content, water adsorption layer and clusters are formed near the slit surface at the water contents of 1.7% and 2.9% respectively. As the total porosity and surface area of the slit model are much larger than those in

the matrix, the reduction of adsorbed gas with the increase of water content in the slit model is much smaller than that in the matrix.

The affinity of gas mixture and water molecules to kerogen is investigated by the radial distribution functions as shown in Fig. 22. Water molecules are mainly distributed near the Oxygen-containing functional group due to the formation of hydrogen bond followed by the Nitrogen- and Sulfur-containing functional groups, while the Carbon-containing functional group is hydrophobic. CO_2 molecules prefer to be adsorbed onto the Sulfur- and Nitrogen-containing functional groups, while CH_4 molecules mainly adsorb on the Carbon- and Sulfur-containing functional groups. The low adsorption affinity of CH_4 to the functional groups result in its higher sensitivity to the water content.

3.3.3. Fluid-kerogen interaction energies

The fluid-kerogen interaction energies at 20 MPa-320 K are shown in Fig. 23. The main interaction energy for water in matrix is lowest at

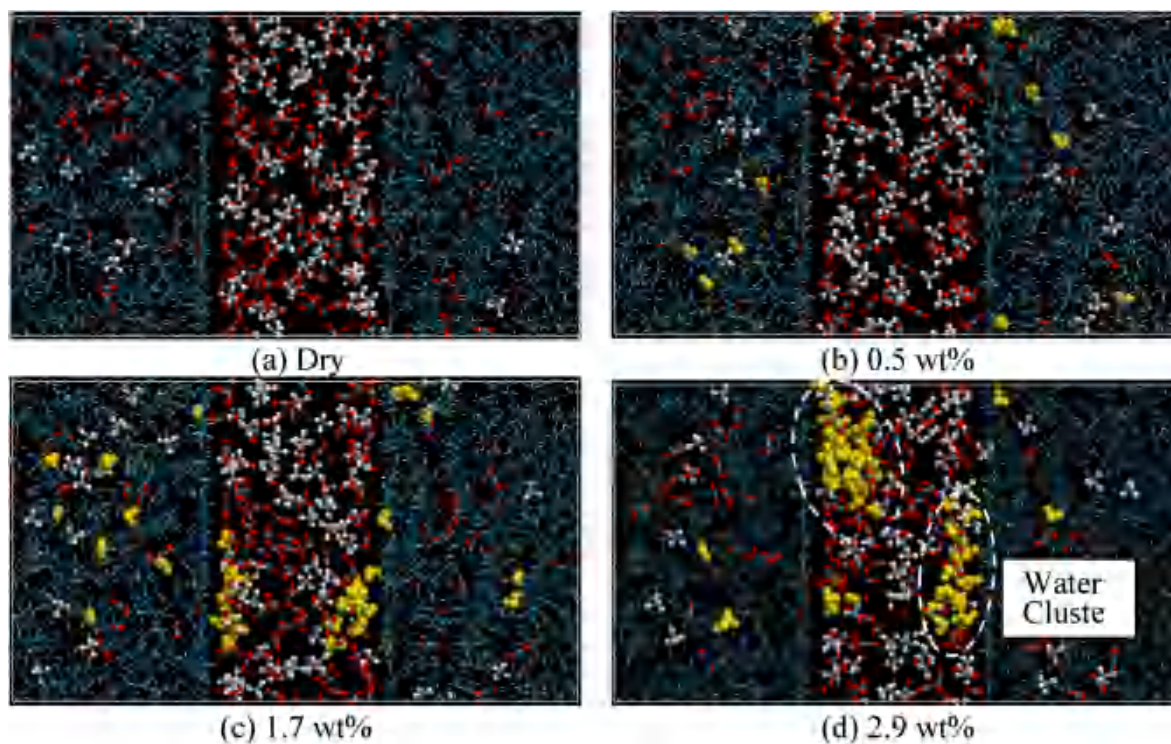


Fig. 21. Distribution of fluid molecules in the kerogen slits at 20 MPa.

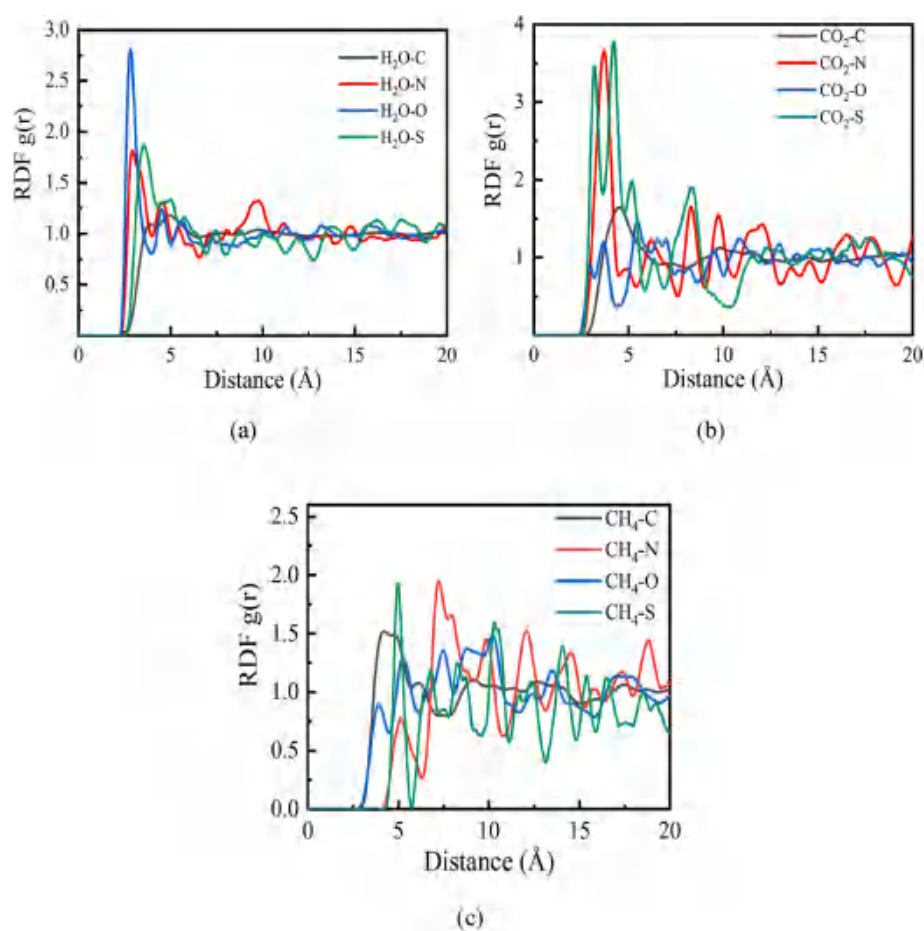
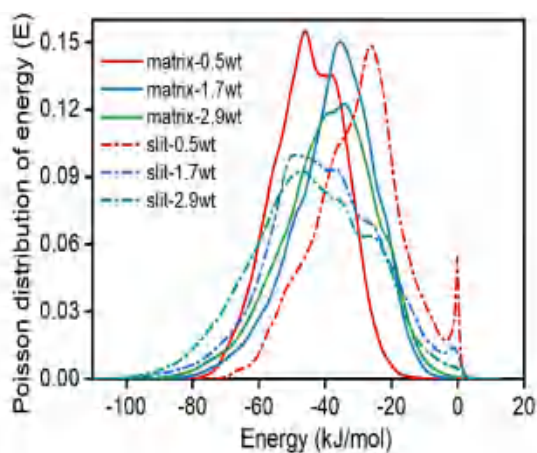


Fig. 22. Radial distribution function of H_2O , CH_4 and CO_2 in kerogen.



(a) Preloaded water

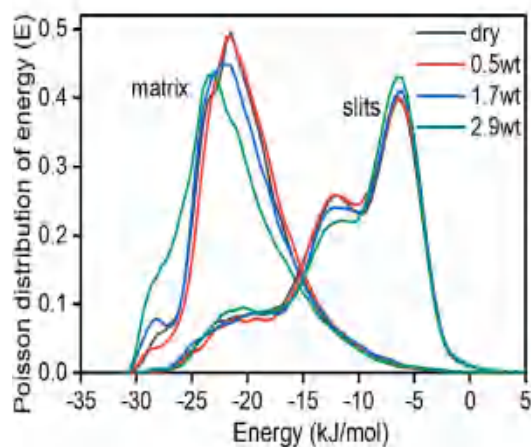
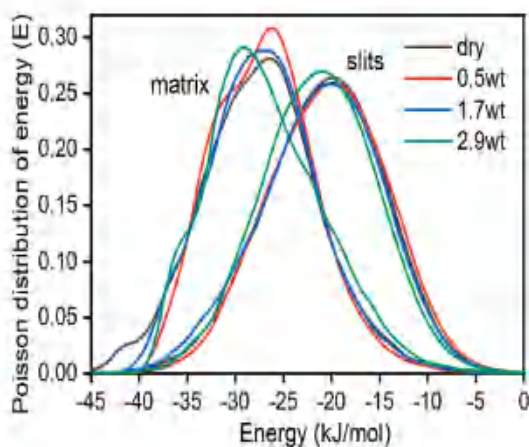
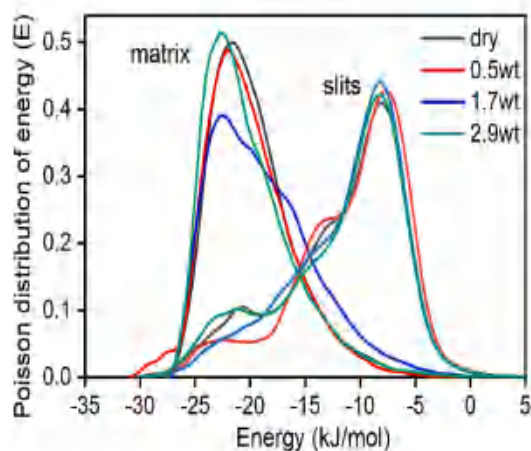
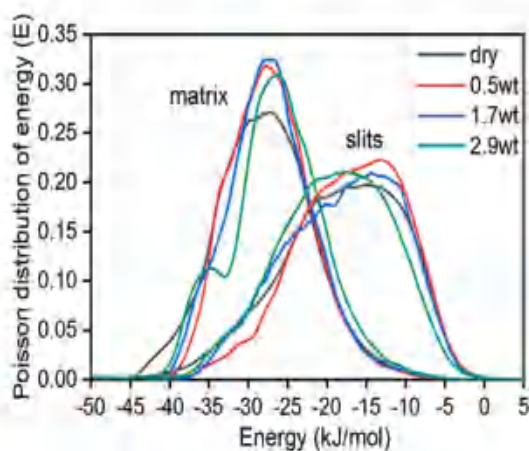
(b) Pure CH₄(c) Pure CO₂(d) CH₄ in equimolar gas mixture(e) CO₂ in equimolar gas mixture

Fig. 23. Interaction energy of pure gas and gas mixture in kerogen matrix and slit with different water contents.

0.5% water content (-46 kJ/mol) due to the superposition of adsorption potential in the nanopores, and it increases to -36 kJ/mol at 1.7% water content as water adsorbs on the secondary adsorption sites. Then it decreases at 2.9% water content due to the formation of water clusters which increases the number hydrogen bond and the binding energy. While the water interaction energy is highest in slit (-26 kJ/mol) at 0.5% water content, which is much larger than those in matrix. And it decreases with the increase of water content due to the formation of water cluster in the slit. As the size of water cluster is much larger than that in matrix pores, significant offset towards the lower interaction energies occurs for the energy distribution curves. The water interaction energies in the slit are comparable with those in the matrix.

The interaction energies for gases in the matrix are always lower than those in the slit due to the adsorption superposition. Generally, the gas energy distribution curves slightly shift to the right at 0.5% water content as water occupies some preferable adsorption sites. And the curves move towards the left with the further increases of water content. This is because the formation of water cluster re-exposes some adsorption sites for gases, and some gas can dissolve or adsorb to water clusters. It should be notified that the CO_2 energy distribution in the leftmost significantly reduces as water occupies the strongest adsorption sites for CO_2 . Water has the strongest adsorption capacity due to the formation of hydrogen bonds, which is also indicated by the lowest interaction energies. CO_2 also displays adsorption preferability compared with CH_4 in terms of interaction energies.

4. Conclusions

The kerogen matrix and slit models are built with the II-A kerogen macromolecules, and the adsorptions of pure CH_4 or CO_2 and their mixtures are modelled by using the GCMC method. The influences of temperature, gas molar fractions and water content on the competitive adsorption are investigated. The following conclusions are obtained.

- 1) CO_2 has larger adsorption capacity compared with CH_4 in both matrix and slit, and the adsorption amounts of CO_2 are 2–3 times and 1–2 times of those of CH_4 in the matrix and slit respectively at equimolar conditions. The adsorption selectivity coefficient ($S_{\text{CO}_2/\text{CH}_4}$) is always larger than unity with high values under low pressures, and it decreases with the increase of CO_2 molar fraction. The higher affinity of CO_2 compared with CH_4 is also verified by the lower interaction energies with kerogen.
- 2) The adsorption of CH_4 and CO_2 in kerogen is physisorption, and they are mainly adsorbed on the Sulfur- and Nitrogen-containing functional groups. Gases are first adsorbed in the matrix pores followed by forming adsorption layer in the slit surface, and finally significant increases in the slit center as free phase, which is consistent with the lower interaction energies in the matrix than that in the slit.
- 3) The presence of water decreased the gas adsorption especially in the matrix as it occupies the Oxygen-containing functional group and displaces the gases in the limited pore space. Besides, CH_4 is more sensitive to the water content as CO_2 can adsorb on the secondary adsorption sites of the water clusters due to the quadrupole moment effect. Water adsorbs on sites with lower interaction energies resulting in the right movement of energy curves at 0.5% water content, while the formation of hydrogen bond and large binding energy in the water cluster result in the left movement of water energy curve at high water contents. In addition, the formation of water cluster also re-expose adsorption sites for gases.

The two-component gas mixture adsorption of CH_4 and CO_2 in dry and moist kerogen slits were simulated in this study, however the real shale gas is a mixture of many components and the injection of CO_2 make interactions more complicated. The adsorption of multiphase and multicomponent fluids in shale pores are suggested for future study to uncover the real fluid storage in shale nanopores.

CRediT authorship contribution statement

Decheng Zhang: Writing – review & editing, Writing – original draft, Supervision, Project administration, Methodology. **Hao Tang:** Writing – review & editing. **Yuqi Song:** Writing – review & editing, Supervision, Methodology. **M.S.A. Perera:** Writing – review & editing. **P.G. Ranjith:** Writing – review & editing.

Declaration of competing interest

The authors declare that they have no known competing financial interests or personal relationships that could have appeared to influence the work reported in this paper.

Data availability

Data will be made available on request.

Acknowledgement

The authors would like to acknowledge the financial support from Natural Science Foundation of China (42202325), Top Young Talents Program of Department of Education of Hebei Province (BJ2021022), China Scholarship Council-Monash University joint project (201708320284), and Australian Research Council Discovery Project (DP220101952).

Abbreviations

GCMC Grand canonical Monte Carlo
COMPASS Condensed-phase Optimized Molecular Potential for Atomistic Simulation Studies

References

- Ansari, H., Gong, S., Trusler, J.P.M., Maitland, G., Pini, R., 2022. Hybrid pore-scale adsorption model for CO_2 and CH_4 storage in shale. *Energy Fuel*. 36 (7), 3443–3456.
- Carchini, G., Al-Marri, M.J., Hussein, I., Shawabkeh, R., Mahmoud, M., Aparicio, S., 2022. Molecular dynamics of CH_4/CO_2 on calcite for enhancing gas recovery. *Can. J. Chem. Eng.* 100 (11), 3184–3195.
- Chen, Z., Farhadian, A., Rizi, Z.T., Mortazavi-Manesh, A., Mohammad-Taheri, M., Aminolroayaei, M.A., Sadeh, E., Chen, C., 2024. Novel core-shell and recyclable gas hydrate promoter for efficient solidified natural gas storage. *Energy Convers. Manag.* 301 (No.0), 118059.
- Curtis, J.B., 2002. Fractured shale-gas systems. *AAPG Bull.* 86 (11), 1921–1938.
- Di Biase, E., Sarkisov, L., 2015. Molecular simulation of multi-component adsorption processes related to carbon capture in a high surface area, disordered activated carbon. *Carbon* 94 (No.0), 27–40.
- Han, Q., Deng, C., Gao, T., Jin, Z., 2022. Molecular simulation on competitive adsorption differences of gas with different pore sizes in coal. *Molecules* 27 (5), 1594.
- Heller, R., Zoback, M., 2014. Adsorption of methane and carbon dioxide on gas shale and pure mineral samples. *Journal of unconventional oil and gas resources* 8, 14–24.
- Hu, W., Chen, C., Sun, J., Zhang, N., Zhao, J., Liu, Y., Ling, Z., Li, W., Liu, W., Song, Y., 2022. Three-body aggregation of guest molecules as a key step in methane hydrate nucleation and growth. *Commun. Chem.* 5 (No.1), 1–11.
- Kim, T.H., Cho, J., Lee, K.S., 2017. Evaluation of CO_2 injection in shale gas reservoirs with multi-component transport and geomechanical effects. *Appl. Energy* 190, 1195–1206.
- Kunz, O., Wagner, W., 2012. The GERG-2008 wide-range equation of state for natural gases and other mixtures: an expansion of GERG-2004. *J. Chem. Eng. Data* 57 (11), 3032–3091.
- Liu, B., Li, X., Qi, C., Mai, T., Zhan, K., Zhao, L., Shen, Y., 2018. Pressure-driven supercritical CO_2 transport through a silica nanochannel. *RSC Adv.* 8 (3), 1461–1468.
- Liu, Y., Zhu, Y., Li, W., Xiang, J., Wang, Y., Li, J., Zeng, F., 2016. Molecular simulation of methane adsorption in shale based on grand canonical Monte Carlo method and pore size distribution. *J. Nat. Gas Sci. Eng.* 30, 119–126.
- Lyu, F., Ning, Z., Yang, S., Mu, Z., Cheng, Z., Wang, Z., Liu, B., 2022. Molecular insights into supercritical methane sorption and self-diffusion in monospecific and composite nanopores of deep shale. *J. Mol. Liq.* 359, 119263.
- Neele, F., Hewson, C., Loeve, D., Eyvazi, F.J., Hegen, D., Hofstee, C., 2018. CO_2 -EGR: using CO_2 to enhance gas or condensate recovery. In: 14th Greenhouse Gas Control Technologies Conference Melbourne.
- Qi, R., 2019. Study on Competitive Adsorption Mechanism of Shale Gas, vol. 520. China University of Petroleum, Beijing (in Chinese).

- Rexer, T.F., Mathia, E.J., Aplin, A.C., Thomas, K.M., 2014. High-pressure methane adsorption and characterization of pores in posidonia shales and isolated kerogens. *Energy Fuel*. 28 (5), 2886–2901.
- Santos, M.S., Franco, L.F.M., Castier, M., Economou, I.G., 2018. Molecular dynamics simulation of n-alkanes and CO₂ confined by calcite nanopores. *Energy Fuel*. 32 (2), 1934–1941.
- Shi, H., 2019. Molecular Simulation of Competitive Adsorption and Diffusion of Shale Gas. China University of Petroleum, East China (in Chinese).
- Shi, Y., Jia, Y., Pan, W., Huang, L., Yan, J., Zheng, R., 2017. Potential evaluation on CO₂-EGR in tight and low-permeability reservoirs. *Nat. Gas. Ind. B* 4 (4), 311–318.
- Singh, H., Javadpour, F., 2016. Langmuir slip-Langmuir sorption permeability model of shale. *Fuel* 164, 28–37.
- Sun, H., 1998. COMPASS: an ab initio force-field optimized for condensed-phase applications overview with details on alkane and benzene compounds. *J. Phys. Chem. B* 102 (38), 7338–7364.
- Sun, J., Chen, Z., Wang, X., Zhang, Y., Qin, Y., Chen, C., Li, W., Zhou, W., 2023. Displacement characteristics of CO₂ to CH₄ in heterogeneous surface slit pores. *Energy & Fuel*. 23, 2926–2944.
- Tang, C., Chen, Z., Farhadian, A., Iravani, D., Chen, C., Song, Y., Rahimi, A., Liang, D., Lu, L., Fan, S., 2024. Environmentally friendly antiagglomerants: a promising solution for gas hydrate plugging and corrosion risk management in oil and gas pipelines. *Energy & Fuel*. 38(8), 6738–6752.
- Ungerer, P., Collett, J., Yiannourakou, M., 2014. Molecular modeling of the volumetric and thermodynamic properties of kerogen: influence of organic type and maturity. *Energy Fuel*. 29 (1), 91–105.
- Wang, T., Tian, S., Li, G., Sheng, M., 2018. Selective adsorption of supercritical carbon dioxide and methane binary mixture in shale kerogen nanopores. *J. Nat. Gas Sci. Eng.* 50, 181–188.
- Wu, J., Huang, P., Maggi, F., Shen, L., 2022. Molecular investigation on CO₂-CH₄ displacement and kerogen deformation in enhanced shale gas recovery. *Fuel* 315, 123208.
- Xie, W., Wang, M., Wang, H., 2021. Adsorption characteristics of CH₄ and CO₂ in shale at high pressure and temperature. *ACS Omega* 6 (28), 18527–18536.
- Yang, N., Liu, S., Yang, X., 2015. Molecular simulation of preferential adsorption of CO₂ over CH₄ in Na-montmorillonite clay material. *Appl. Surf. Sci.* 356 (No.1), 1262–1271.
- Yu, H., Xu, H., Fan, J., Zhu, Y.-B., Wang, F., Wu, H., 2020. Transport of shale gas in microporous/nanoporous media: molecular to pore-scale simulations. *Energy Fuel*. 35 (2), 911–943.
- Zeng, K., Jiang, P., Lun, Z., Xu, R., 2018. Molecular simulation of carbon dioxide and methane adsorption in shale organic nanopores. *Energy Fuel*. 33 (3), 1785–1796.
- Zhang, D., Gao, H., Ranjith, P.G., Zhang, C., Ma, G., 2022a. Experimental and theoretical study on comparisons of some gas permeability test methods for tight rocks. *Rock Mech. Rock Eng.* 55, 3153–3169.
- Zhang, D., Ranjith, P., Perera, M., Ma, G., 2020a. Laboratory evaluation of flow properties of Niutitang shale at reservoir conditions. *Mar. Petrol. Geol.* 115, 104257.
- Zhang, D., Ranjith, P., Perera, M., Zhang, C., 2020b. Influences of test method and loading history on permeability of tight reservoir rocks. *Energy*, 116902.
- Zhang, D., Tang, H., Zhang, X., Ranjith, P., Perera, M., 2022b. Molecular simulation of methane adsorption in nanoscale rough slits. *J. Nat. Gas Sci. Eng.*, 104608.
- Zhang, H., Cao, D., 2016. Molecular simulation of displacement of shale gas by carbon dioxide at different geological depths. *Chem. Eng. Sci.* 156, 121–127.
- Zhao, T., Li, X., Zhao, H., Li, M., 2017. Molecular simulation of adsorption and thermodynamic properties on type II kerogen: influence of maturity and moisture content. *Fuel* 190, 198–207.
- Zhou, W., Zhang, Z., Wang, H., Yang, X., 2019. Molecular investigation of CO₂/CH₄ competitive adsorption and confinement in realistic shale kerogen. *Nanomaterials* 9 (12), 1646.